This article has been accepted for publication in a future issue of this journal, but has not been fully edited. Content may change prior to final publication. Citation information: DOI 10.1109/TTE.2019.2920328, IEEE Transactions on Transportation Electrification

Integration of Magnified Alternating Current in Battery Fast Chargers based on DC-DC Converters using Transformerless Resonant Filter Design

Rudi Soares, *Student Member IEEE*, Nikolina Djekanovic, *Student Member IEEE*, Oskar Wallmark, *Senior Member IEEE*, and Poh Chiang Loh, *Senior Member IEEE*

***Abstract*—For safety and longevity reasons, in subzero temperatures, lithium-ion batteries can only be charged after pre-commissioning their temperature. Therefore, in such conditions fast charging depends on fast heating. Recently, the injection of AC currents into lithium-ion batteries has been reported as a technique with potential to decrease heating time. This paper proposes a method based on a multi-objective algorithm for DC-DC converter design using transformerless resonant filters. The method enables the DC-DC converters to produce magnified AC current in addition to the DC current. Using the proposed design method, a topological survey of DC-DC converters with magnified AC current capability composed of either half- or full-bridge switch arrangements is carried out. In the presented experimental setup, it is demonstrated that by using an LCL circuit with specific component values and a full-bridge switch arrangement, magnifications of up to 15.7 may be reached. Further, by matching the switching frequency with the frequency where the LCL and the battery resonate, for the same injected AC current, the current flowing in the semiconductors and the switching frequency could be reduced. This allowed a loss reduction in the semiconductors of up to 75%, when compared with an equivalent DC-DC converter enabled to produce a non-magnified AC current.**

***Index Terms*—Batteries, DC-(DC/X·AC) converters, fast charging, fast heating, injection of alternating current.**

I. Introduction

Lithium-ion batteries (LIBs) experience significant loss in power capability and rapidly age if charged with direct current (DC) at subzero temperatures [1]–[5]. This means that in subzero climates fast charging depends on fast heating, since charging should only happen after pre-heating the LIB.

Today, LIB heaters include the use of a circuit of fluid, a heater, a pump, and dedicated electronics. They are slow since they highly depend on the LIB packaging, and can only heat-up the LIB cell's surface. Subsequently, the temperature distribution throughout the LIB cell's body takes time spreading evenly, and if not well addressed, localized fatigued points will appear in the cells. To solve these issues, the authors in [6] advocated for the injection of alternating current (AC) as a potentially better solution for heating LIBs. Since then, this technique has received considerable attention in [7]–[12]. Heating a LIB by injecting AC current results in evenly distributed temperature and requires virtually no hardware changes in DC-DC converters (already existing charging hardware). Moreover, when compared with conventional heaters, this technique has shown to require less time and less energy to rise the temperature for one Celsius degree in a LIB [13]. In [11] the authors demonstrated that with the injection of an AC current with an amplitude of 3.1 c-rate and a frequency of 833 Hz, the LIB cell under study could be heated up from -20 °C to 0 °C in 5.9 minutes. Despite of the attractiveness of this result, a demonstration of such performance considering a LIB packaging (and its influence in the overall thermal inertia) is still necessary to completely show the commercial viability of this technique.

This paper contributes to the development of this technique by proposing a DC-DC converter design method which optimizes converter performance during the injection of an AC current into LIBs. To integrate large AC current capability into DC-DC converters used for LIB fast charging, this paper proposes the use of transformerless resonant filters as AC current magnifiers. This converter type is here called DC-(DC/X·AC) converter, where X corresponds to the magnification gain experienced by the AC current. This is achieved by exciting the output filter and the LIB with their resonant frequency. Otherwise, as usual in DC-DC converters, the filter behaves as a current ripple attenuator. The calculation of the DC-(DC/X·AC) converter's specifications, such as, operating frequency and component sizes, is accomplished using a multi-objective algorithm. In this paper, the two objectives used in the algorithm are: maximize the AC current magnification and minimize the circuit impedance. However, these objectives serve a higher purpose which is to maximize the generated heat in the battery while minimizing converter losses. Further, the usage of multi-objective algorithms allows the inclusion of additional objectives into the design process. Since this converter type drives AC current at the resonant frequency, only active power is consumed, meaning that no reactive power compensation is required.

Depending on the converter size and its usage, in electrical vehicle (EV) charging applications, the semiconductor losses may account for the largest part of the losses in a DC-DC converter [14]. For instance, in [15], in a studied 50 kW

Rudi Soares is the corresponding author of this paper. He is with the Department of Electric Power and Energy Systems, KTH Royal Institute of Technology, SE-100 44 Stockholm, Sweden. Contacts, e-mail: rhsoares@kth.se and tel.:+46-72-9494-905.

Nikolina Djekanovic and Oskar Wallmark are with the Department of Electric Power and Energy Systems, KTH Royal Institute of Technology, SE-100 44 Stockholm, Sweden (e-mails: ndje@kth.se, owa@kth.se).

Poh Chiang Loh is with the Department of Electronic Engineering, Chinese University of Hong Kong, Rm 427, Ho Sin Hang Engineering Building, Hong Kong (e-mail: pcloh@ee.cuhk.edu.hk).

This article has been accepted for publication in a future issue of this journal, but has not been fully edited. Content may change prior to final publication. Citation information: DOI 10.1109/TTE.2019.2920328, IEEE Transactions on Transportation Electrification

voltage source converter (VSC), 60% of the overall converter losses (namely, losses of the input filter, semiconductors and the output filter) arose in the semiconductors of the converter. This makes the losses in the semiconductors the first target in the optimization of converters for fast chargers and it is the primary reason why DC-(DC/X·AC) may be more interesting for production of large AC currents than oversized DC-(DC/AC) converters.

Historically, and still today according to some papers, AC currents have been regarded as harmful for LIBs [16]–[19]. However, recently [20]–[24] show that AC currents may not be as harmful for LIB as considered so far. Nonetheless, [20]–[24] did not carry experimental tests with AC currents higher than 1 c-rate, and their conclusions still need confirmation for subzero temperatures. However, in case large AC currents injected at subzero temperatures turn out not to be harmful for LIBs, DC-(DC/X·AC) converters may be a good candidate for tomorrow's fast chargers.

To demonstrate the flexibility of the design method proposed, in this paper four converter configurations are modeled, implemented in an experimental setup, and analyzed in a battery heating context. Namely, three DC-(DC/X·AC) converters: 1) half-bridge driving a resonant filter (LCL); 2) full-bridge driving a resonant filter (LCL); 3) full-bridge driving a resonant filter (LCL) where the switching frequency is the resonant frequency, and a DC-(DC/AC) converter, i.e., half-bridge driving an inductor with no AC current magnification. The last converter is used as a benchmark case, i.e., it is designed to be a reference at the three DC-(DC/X·AC) converters comparison.

II. Heat generated by injecting AC current

The rate of the heat generated in the interior of a LIB cell, $\dot{q}$ [W], may be categorized as entropic or ohmic heat [25]. Entropic heat is caused by electrochemical processes named by charge transfer overpotential, and by mass transfer overpotential. These processes are slow, and typically happen for currents with frequencies below 1 kHz [26], [27]. In contrast, ohmic heat occurs regardless of the frequency of the current flowing in the LIB. It is dependent on the real part of the LIB's impedance (addressed as $\Re(Z_{\text{batt}})$) at a certain frequency and certain temperature, and the root-mean-square value of the injected AC current amplitude (i_{rms}). In this paper, the injected AC currents are always targeted at frequencies higher than 1 kHz and, therefore, the rate of generated heat can be expressed as

$$\dot{q} = \Re(Z_{\text{batt}}) i_{\text{rms}}^2 \ . \tag{1}$$

Since for lower frequencies the real part of the LIB cell impedance increases, frequencies below 300 Hz have been preferred in [7]–[10], [12], [13]. Nonetheless, considering that the rate of generated heat is affected by the power of two of the injected AC current, the AC current magnification, which is achieved by the DC-(DC/X·AC) type of converter and explained in the Introduction, may be a more effective way to generate heat in the interior of LIBs than reducing the frequency of the injected current.

III. Electric modeling

A. Battery Model

Electrochemical impedance spectroscopy (EIS) measurements were carried out in order to build an impedance model of the battery cell. The measurements are performed on a large (28 Ah) prismatic LIB cell optimized for high power density. The measurements were performed with the LIB cell mounted into pressure plates, at 3.67 V (corresponding to a state of charge (SOC) level of 50 %), and in ambient temperature which was approximately 20 °C. The data were collected using a frequency response analyzer with a variable step (Zahner IM6 KG), operated with a voltage perturbation of 10 mV and with a frequency sweep from 10 kHz down to 100 mHz. The number of points per decade was set to 10.

The electrical dynamics of LIBs may be represented using equivalent electric circuits as well as transfer functions [28]–[31]. In this paper, an approximated transfer function with two poles and two zeros, as shown in (2), is obtained by fitting of the measured cell impedance data and is expressed by

$$Z_{\text{cell}}(s) \approx \frac{(n_2 s^2 + n_1 s + n_0)}{(s^2 + d_1 s + d_0)} \tag{2}$$

where n_k and d_k are the numerator and denominator model coefficients of the LIB cell under study, with $k = 0, 1, 2$. With n_{ser} and n_{par} terms as the numbers of (assumed identical) cells in series and parallel composing the LIB pack, the total battery pack impedance can be approximated using the following transfer function

$$Z_{\text{batt}}(s) = \frac{n_{\text{ser}}}{n_{\text{par}}} Z_{\text{cell}}(s). \tag{3}$$

The EIS data can be found in Figure 1 in a form of a Nyquist plot (blue line). Due to the interest in frequencies higher than 1 kHz, and in order to improve the fit quality of the modeled region, the fit is narrowed down by selecting the EIS data points from 1 kHz to 10 kHz (red line). The fit results (pink line), which are used to obtain the cell model are plotted on top of the first two lines. As it may be observed for frequencies higher than 1 kHz the LIB cell behaves mainly as an inductor in series with a resistor.

In a state-space representation, $Z_{\text{cell}}(s)$ could be rewritten as

$$\begin{aligned} \dot{\mathbf{x}}_{\text{b}} &= \mathbf{A}_{\text{b}} \mathbf{x}_{\text{b}} + \mathbf{b}_{\text{b}} u \\ y &= \mathbf{c}_{\text{b}}^T \mathbf{x}_{\text{b}} + d_{\text{b}} u \end{aligned} \tag{4}$$

with the input ($u = i_{\text{batt}}$) as the current entering the cell, while the output ($y = u_{\text{batt}}$) is given by the cell voltage. The poles of the transfer function $Z_{\text{cell}}(s)$ correspond to the eigenvalues of the system matrix $\mathbf{A}_{\text{b}}$ of the presented state-space model. Therefore, the number of states needed to describe the cell impedance is two and they are given by the following state vector

$$\mathbf{x}_{\text{b}} = \begin{bmatrix} x_1 & x_2 \end{bmatrix}^T . \tag{5}$$

This type of representation is chosen in order to calculate the ratio between the battery cell current and the input current,

This article has been accepted for publication in a future issue of this journal, but has not been fully edited. Content may change prior to final publication. Citation information: DOI 10.1109/TTE.2019.2920328, IEEE Transactions on Transportation Electrification

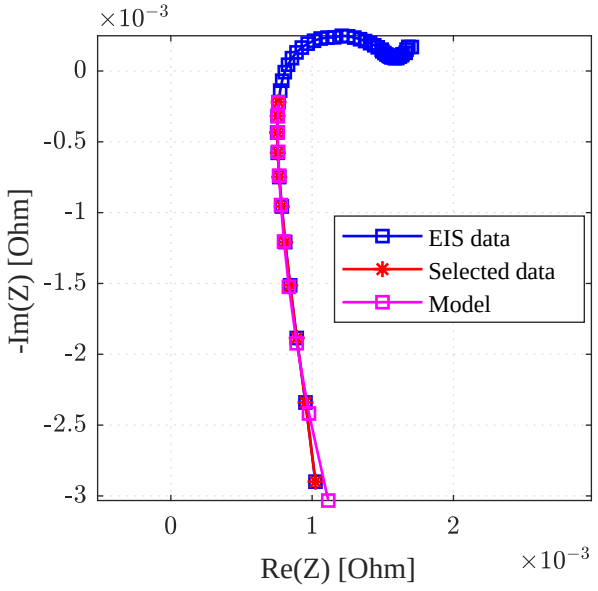

Figure 1. Plot of the electrochemical impedance spectroscopy data in a frequency range from 100 mHz to 10 kHz, selected data for the fit, and LIB cell modeled.

as described in more detail in Section IV-A. From (4), the following relation holds

$$u_{\text{batt}} = \mathbf{c}_{\text{b}}^T \mathbf{x}_{\text{b}} + d_{\text{b}} i_{\text{batt}}. \tag{6}$$

This further sets the dimensions of the matrix and the vectors in (4) to $\mathbf{A}_{\text{b}} \in \mathbb{R}^{2\times 2}, \mathbf{b}_{\text{b}}, \mathbf{c}_{\text{b}} \in \mathbb{R}^{2\times 1}, d_{\text{b}} \in \mathbb{R}$.

B. Impedance Modeling of the LIB and Resonant Filter

The schematics of the circuits investigated are presented in Figure 2, which is divided in four subfigures corresponding to each of the configurations. Note that, the first three subfigures a) - c) share the same LCL filter and LIB construction.

Typically, when VSCs are used to control the current in a battery, the switched voltage output of the VSC needs to be filtered. The inductor, L_1 and its parasitics R_{L1} from Figure 2, are placed in series with the battery in order to reduce the current ripple due to the switching action. Since L_1 is assembled at the switches' output, and the battery is often located at a distance, power cables (represented in Figure 2 by L_2 and its parasitics R_{L2}) are required. Now, considering that the existence of L_1 and L_2 is inescapable, the closest resonant filter topology to investigate is the LCL. Simply by designing and placing a capacitor (C_{r} and its parasitics R_{C} from Figure 2) in parallel with the battery (Z_{batt} from Figure 2) a DC-DC converter may be operated as a DC-(DC/X·AC) converter.

In order to derive an overall impedance model of the LIB and resonant filter in a state-space form, Kirchhoff's current law (KCL) and voltage law (KVL) are applied to the right part of the subfigure a) in Figure 2. The model is derived by combining the state-space model of the LIB from (4) and the differential equations obtained by reorganizing the KCL and KVL expressions. The corresponding state vector of the overall model together with the differential equations are given below

$$\mathbf{x}_{\text{I}} = \begin{bmatrix}\mathbf{x}_{\text{b}} & i_{\text{in}} & u_c & i_{\text{batt}}\end{bmatrix}^T, \tag{7}$$

$$\frac{di_{\text{in}}}{dt} = \frac{1}{L_1}\left(u_{\text{in}} - R_{L1} i_{\text{in}} - R_C(i_{\text{in}} - i_{\text{batt}}) - u_c\right), \tag{8}$$

$$\frac{du_c}{dt} = \frac{1}{C_r}\left(i_{\text{in}} - i_{\text{batt}}\right), \tag{9}$$

$$\frac{di_{\text{batt}}}{dt} = \frac{1}{L_2}(u_c - u_{\text{batt}} - E_{\text{batt}} - R_{L2} i_{\text{batt}}) + \\ + \frac{R_C}{L_2}(i_{\text{in}} - i_{\text{batt}}). \tag{10}$$

The input and the output of the impedance model are defined as

$$\mathbf{u} = \begin{bmatrix}u_{\text{in}} & E_{\text{batt}}\end{bmatrix}^T, \qquad \mathbf{y} = \begin{bmatrix}i_{\text{in}} & i_{\text{batt}}\end{bmatrix}^T. \tag{11}$$

The remaining parameters are explained in more detail in the following section. Note that, compared to the model of the LIB and the resonant filter, the input of the cell impedance model is a current, whereas the output is a voltage, according to (6). In order for the overall model to consider charging of the battery, a second input voltage corresponding to the LIB's current SOC (E_{batt}) is included.

IV. Multi-objective optimization design method

The proposed design method allows the designer to explore the synergies rising from the integration of the *DC* and the *X·AC* features in a single converter. Hence, the component values L_1, L_2, C_r, and the operating frequency (here called f_{op}), are considered optimizable within certain constraints. In Sections IV-A and IV-B, the analytical background necessary to derive the objective functions, i.e., maximization of the produced AC current magnification and minimization of the overall impedance is presented.

A. Maximizing the Magnification

With the purpose of reducing the current in the semiconductors, and yet in order to reach large LIB currents, magnification of the AC current is proposed. It can be defined as the ratio between the fundamental magnitude of the LIB current (called i_{batt}), and fundamental magnitude of the VSC's output current, which is subsequently the input of the resonant filter (here called i_{in}). Both currents may be found in Figure 2. This ratio is given by the transfer function and it will be referred to as the Gain transfer function

$$G_{\text{Gain}}(s) = \frac{I_{\text{batt}}(s)}{I_{\text{in}}(s)}. \tag{12}$$

The expressions $I_{\text{batt}}(s)$ and $I_{\text{in}}(s)$ stand for Laplace transforms of the currents i_{batt} and i_{in}, respectively. $I_{\text{batt}}(s)$ and $I_{\text{in}}(s)$ may be obtained by using the state-space model of the circuit, presented in Sections III-A and III-B. The corresponding transfer function $G(s)$ of the overall model is a 2x2 matrix, as can be concluded from (11), and it can be used to calculate the Gain transfer function as

$$G_{\text{Gain}}(s) = \frac{G_{2,1}(s)}{G_{1,1}(s)} \tag{13}$$

This article has been accepted for publication in a future issue of this journal, but has not been fully edited. Content may change prior to final publication. Citation information: DOI 10.1109/TTE.2019.2920328, IEEE Transactions on Transportation Electrification

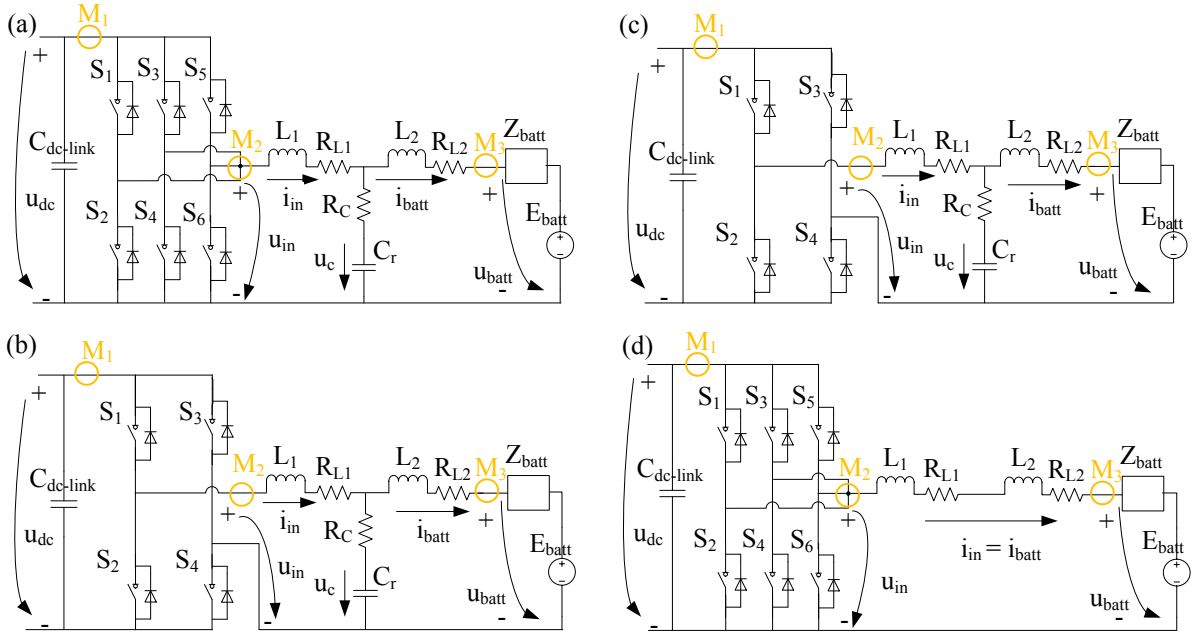

Figure 2. Circuit schemes of the four investigated configurations: a) half-bridge driving i_{in} into an LCL using PWM; b) full-bridge driving i_{in} into an LCL using PWM; c) full-bridge driving i_{in} into an LCL, where the switching frequency is the resonant frequency; d) half-bridge driving i_{in} into an inductor using PWM. The yellow M1, M2 and M3 symbols point the locations of current and voltage measurements.

with

$$G_{1,1}(s) = \frac{Y_1(s)}{U_1(s)} = \frac{I_{\text{in}}(s)}{U_{\text{in}}(s)}, \qquad \text{and} \tag{14}$$

$$G_{2,1}(s) = \frac{Y_2(s)}{U_1(s)} = \frac{I_{\text{batt}}(s)}{U_{\text{in}}(s)}. \tag{15}$$

B. Minimizing the Impedance

The LCL filter topology comprises an inductor (L_1) in series with a parallel resonant connection, namely between a capacitor C_r, and an inductor L_2 (with all the respective parasitics) and the battery Z_{batt}. To avoid possible VSC's output voltage saturation, the overall impedance of the circuit Z_{imp} at the operating frequency should also be kept minimal. Simply by observing Ohm's law,

$$u_{\text{in}} = Z_{\text{imp}}\ i_{\text{in}} \tag{16}$$

one may conclude that for a given VSC output voltage (u_{in}) the maximum possible output current of the VSC is a function of Z_{imp}. By falling into voltage saturation, the current i_{in} (even if not yet magnified) will be smaller than the one requested by the controller. The principles behind this problem are similar to the ones known as the boundary between continuous and discontinuous mode in DC-DC converters [32].

As addressed in Section IV-A the Z_{imp} is given by the inverse of the transfer function $G_{1,1}(s)$, and can be translated to the following expression

$$Z_{\text{imp}}(s) = \frac{\left(R_C + \frac{1}{sC_r}\right)(R_{L2} + sL_2 + Z_{\text{batt}})}{R_C + \frac{1}{sC_r} + R_{L2} + sL_2 + Z_{\text{batt}}} + \\ + R_{L1} + sL_1. \tag{17}$$

C. Multi-Objective Algorithm Implementation

In parallel resonant circuits, current magnification is achieved at the expense of an impedance that tends theoretically to infinity. Therefore, maximizing current gains (according to (23) in Appendix A) means that the overall impedance (presented in (17)) will inevitably increase. On the other hand, increasing the circuit's impedance means sacrificing the maximum VSC's output current. Therefore, a compromise between gain and impedance needs to be established. To fulfill these two antagonistic aims, the following two objective functions need to be minimized at the same time:

1) Reversed Gain transfer function (Equation (23)),
2) Absolute impedance of the whole circuit (Equation (17)).

To address this issue, a multi-objective algorithm is proposed. The optimization process can be summarized as:

$$\underset{x}{\text{minimize}} \quad f(x),\ g(x) \tag{18}$$

$$\text{subject to} \quad B_l \leq x \leq B_h \tag{19}$$

For simplicity, the stray resistances (R_{L1}, R_C, R_{L2}) are considered constant, while the set of parameters that needs to be determined is given by $x = \{\omega_{\text{op}}, L_1, L_2, C_{\text{r}}\}$. B_l

This article has been accepted for publication in a future issue of this journal, but has not been fully edited. Content may change prior to final publication. Citation information: DOI 10.1109/TTE.2019.2920328, IEEE Transactions on Transportation Electrification

and B_h are the lower and the upper boundaries of these parameters. An example of the algorithm implementation is given in Section VI. The minimization functions are given as

$$f(x) = \left| \frac{1}{G_{\text{Gain}}(x)} \right|, \quad g(x) = |Z_{\text{imp}}(x)| \tag{20}$$

with G_{Gain} defined in (23) and Z_{imp} in (17). The proposed method implementation is based on genetic algorithms, which were selected in order to maximize the probability of finding global minima [33]. Specifically, appropriated values of population size and number of iterations were selected to ensure that the algorithm would maximize the diversity of the population between successive generations. A special advantage of this method is that no initial conditions are required.

The optimization method output is known as a Pareto front. Figure 3 is an example of the Pareto front obtained from the above described method using Matlab[1] and the function gamultobj. Each point on the Pareto front corresponds to an optimal parameter set $x = \{\omega_{\text{op}}, L_1, L_2, C_{\text{r}}\}$ for the given pair of objectives. Now, considering (12) in conjunction with (16), the magnified AC current may be included as a target for the Pareto front search and its Laplace transform can be expressed as

$$I_{\text{batt}}(s) = \frac{u_{\text{in}} G_{\text{Gain}}(s)}{Z_{\text{imp}}(s)}. \tag{21}$$

For example, assuming that the target (for instance, safe upper limit of AC current from a given LIB cell) i_{batt} is 100 A_{peak} and $u_{\text{batt}} = 50$ V, $u_{\text{dc}} = 100$ V. For the selected optimum shown in Figure 3, where the gain / impedance are 6.2 and 2.5 Ω respectively, the maximum current $i_{\text{in}} = 50$ V /2.5 Ω = 20 A leads to $i_{\text{batt}} = 124$ A. However, still many points of the Pareto front satisfy the presented example. This leaves margin to reiterate the optimization of the multi-objective algorithm privileging either gain maximization (zone marked with green color in Figure 3) or impedance minimization (zone marked with orange color in Figure 3). Thereby, the selected values $\omega_{\text{op}}, L_1, L_2, C_{\text{r}}$ are adjusted as well.

V. Experimental Setup

The experimental setup uses a VSC designed to act as a charger (producing DC current only) as well as a heater (producing AC current only). In order to test with different switch arrangements (namely, half- and full-bridge), the designed VSC is a three-phase converter equipped with six IPP120N20NFD MOSFETs from Infineon[2]. The MOSFETS can handle 200 V nominally and are capable of continuously delivering 20 A with the present heatsink. When the three-phase legs are connected in parallel, this configuration allowed the VSC to continuously generate ±60 A. Figure 4 shows the experimental setup design used for this paper.

The LIB cells considered for the experiments are power optimized NMC prismatic cells, intended for a traction application with a capacity of 28 Ah. For the tests presented in this

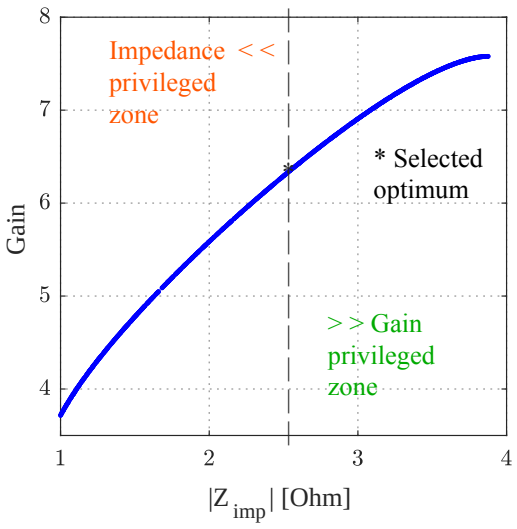

Figure 3. Pareto front as a result of the optimization method performed for the half-bridge configuration.

paper, five LIB cells were connected in series. Considering a voltage per cell of 3.67 V (at 50% SOC), the nominal voltage of the LIB pack is 18.35 V. The VSC is fed by a 48 V DC controllable power supply from TDK Lambda Z+ connected in parallel with a lead-acid battery, which is further connected in parallel with the DC-link of the VSC. This configuration enables the charge cycle currents to flow back-and-forth, i.e., from the lead-acid battery to the cells as well as from the cells to the lead-acid battery. This made the setup more energy efficient, since the 48 V power supply only needs to compensate for the losses of the charge cycle process or when the VSC is producing AC current only.

The VSC is controlled using the microcontroller TMS320F28065 Picolo™ from Texas Instruments allowing a switching frequency of up to 70 kHz. The TMS320F28065 Picolo™ was programmed in C-language using Code Composer Studio[3]. In turn the microcontroller's 5 V output logic signals are driven via the FAN7390M1X from Fairchild[4] to the MOSFETs which receives the signal as 15 V signals. The result of the MOSFETs switching action may be visualized in Figure 6. The communication between the VSC and the rest of the setup is done via controller area network (CAN) protocol. The NI cDAQ 9174 chassis from National Instruments[5] was selected to collect the measured voltage at the LIB with the help of NI 9215 card, whereas the CAN bus used the NI 9862 card. The VSC's generated AC current (processed at the microcontroller) is either achieved using a close-loop current control and pulse width modulation (PWM), or by switching without modulation. In the latter case the current may be controlled by changing the voltage fed to the VSC. Finally, the VSC's output current drives the chosen filter (resonant or not). Figure 6 shows the setup's

[1]Matlab and Simulink are registered trademarks of The Mathworks, Natick, MA, U.S.A.

[2]Infineon Technologies AG, Neubiberg, Germany.

[3]Code Composer Studio is a registered trademark of Texas Instruments, Dallas, TX, USA.

[4]Fairchild Semiconductor International, Inc., Sunnyvale, California, USA.

[5]National Instruments Corporation, Austin, TX, USA.

This article has been accepted for publication in a future issue of this journal, but has not been fully edited. Content may change prior to final publication. Citation information: DOI 10.1109/TTE.2019.2920328, IEEE Transactions on Transportation Electrification

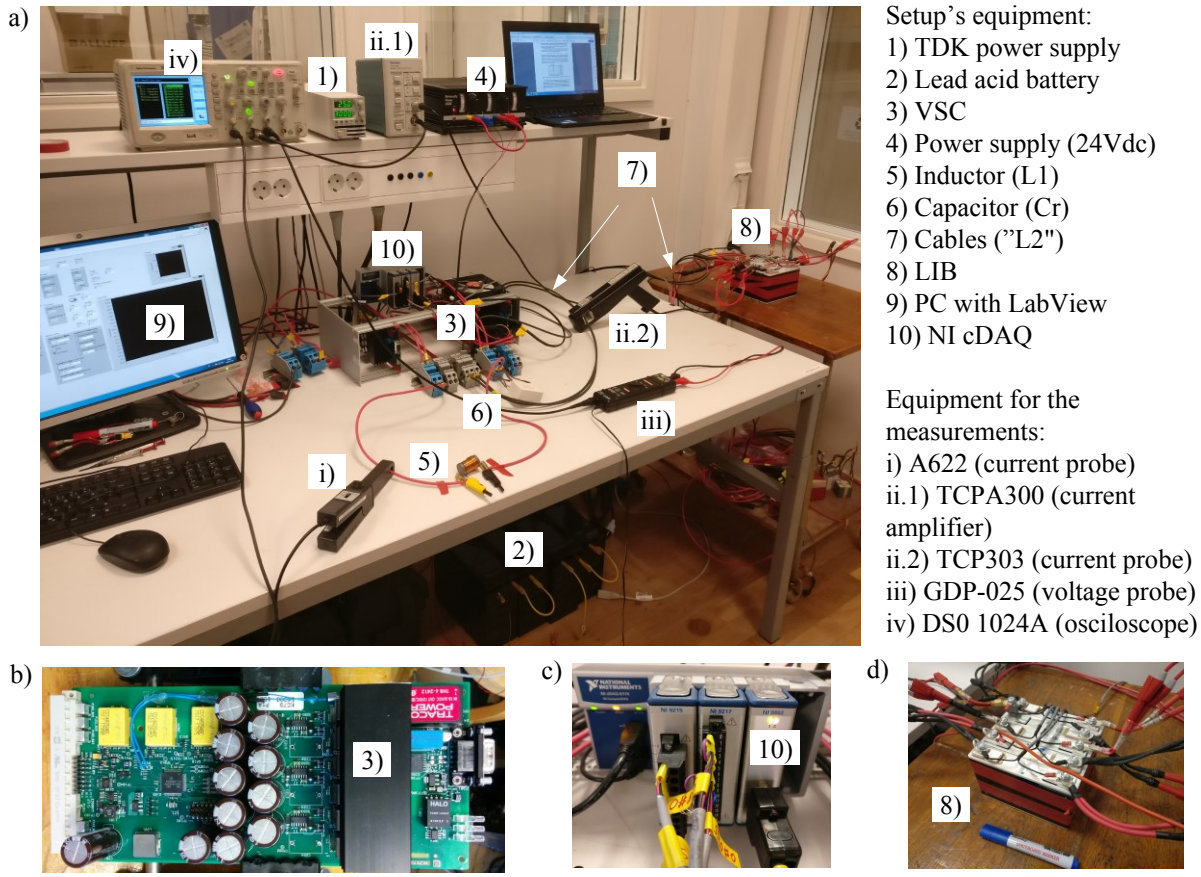

Figure 4. Experimental setup: (a) global view; (b) zoom in on the VSC; (c) zoom in on the NI acquisition system; (d) zoom in on the LIB pack.

VSC injecting 28 A at different frequencies in the LIB pack under study.

VI. Gain spectroscopy validation example

As an example, a set of parameter values is chosen using the described optimization method in Section IV-C, in order to verify the validity of its outcome with both simulations and experiments.

The gain spectroscopy (GS) is performed by the experimental setup's VSC in full-bridge configuration, without the LIB cell in the circuit, by injecting a controlled modulated current. It is essentially a chirp current signal similar to the one used for the regular EIS (shown in Section III-A). The difference is that instead of measuring voltage and current and then calculating the impedance, in case of a GS, two currents are measured and their ratio is determined over a certain frequency range. The obtained measurements are processed in Matlab and thereby the fast Fourier transform (FFT) analysis of both current signals is performed. Only the ratio of the fundamental components is considered as the gain. The commercial filter component values used for the validation slightly differed from the ones designed through the optimization method. Hence, the method is repeated, this time narrowing the upper and lower boundaries (B_h, B_l) of the parameter set x around the measured component values. Moreover, the stray resistance values were then updated in the optimization. The exact values of the resonant components used for the conducted experiment are measured with Rohde & Schwarz HM8118 Programmable LCR Bridge using a signal of 1 kHz. Table I gathers both theoretical and experimental values used in the GS validation example.

Table I
Parameter values obtained from the optimization compared with the measured component values used in the experiment.

Parameter	Optimization	Experiment
f_{op} [Hz]	2034.6	2030
L_1 [mH]	3.79	3.78
R_{L1} [mΩ]	380	372
L_2 [μH]	210	208
R_{L2} [mΩ]	55	35.5
C_{r} [µF]	28.6	29.9
R_C [mΩ]	15	7.3
Gain	31	30.6

In order to further validate the optimization outcome by simulation, a PLECS[6] (Simulation Platform for Power Electronic

[6]PLECS is a registered trademark of Plexim GmbH.

This article has been accepted for publication in a future issue of this journal, but has not been fully edited. Content may change prior to final publication. Citation information: DOI 10.1109/TTE.2019.2920328, IEEE Transactions on Transportation Electrification

Systems) model of the experimental setup was constructed. However, the impedances of the assembled LCL filter used in the experiment marginally differed from the ones in the PLECS model, which uses lumped elements, that for simplicity are not frequency dependent. This is to be expected since contact resistances are added, and the frequency of the injected AC current is slightly different from the one used for the Rohde & Schwarz HM8118 measurement. Subsequently, the exact resonant frequency point may marginally deviate from the one predicted through the optimization and simulated with PLECS. In other words, the designed resonant frequency point in practice is not an exact point, but it is rather a narrow frequency band. The better the Z_{imp} estimation, the more accurate the resonance (targeted frequency point and experienced gain) will be. Further, the results of the GS can be seen in the Bode plot of both simulation and experimentally obtained data, given in Figure 5.

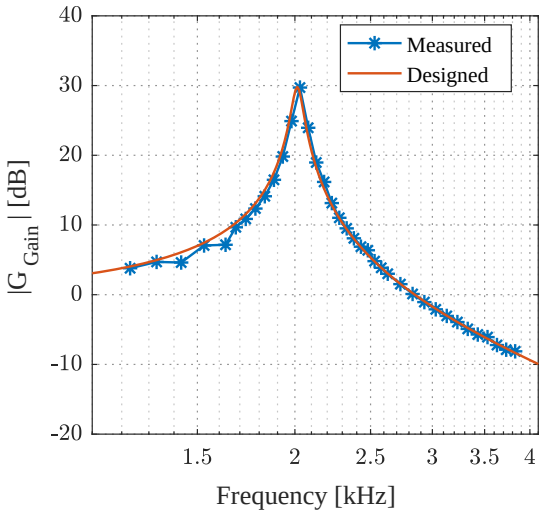

Figure 5. Comparison of Bode plots of G_{Gain} for experimental and simulation results.

VII. Topological Survey and Validation of the Design Method

According to Figure 2, and as stated in the Introduction, four test cases are explored in this paper: 1) half-bridge driving a resonant filter (LCL) using PWM for the current control at the i_{in} signal; 2) full-bridge driving a resonant filter (LCL) using PWM for the current control at the i_{in} signal; 3) full-bridge driving a resonant filter (LCL) where the switching frequency is the resonant frequency, meaning that no current modulation is used; and finally 4) half-bridge driving an inductor with no AC current magnification, using PWM for the current control at the i_{in} signal. Note that, in case (3), to ensure zero DC current, a current controller was programmed so that the ratio between u_{batt} and u_{dc} was checked and corrected.

In order to validate the gains achieved by the designed $x = \{\omega_{\text{op}}, L_1, L_2, C_{\text{r}}\}$ the first three respective configurations were simulated in Matlab/Simulink and PLECS and implemented in the experimental setup. Figure 6 shows the results achieved using the experimental setup. Since there is no current magnification in the case 4) i.e., the gain is 1, no measurements were plotted here. Note that in all the plots, the blue signal stands for the voltage u_{in}, the orange signal for the current i_{in}, whereas the orange dashed signal represents the LIB current. Moreover, Table II gives an overview of the operating frequencies, designed LCL components and their stray resistances, and finally the achieved gains for the studied configurations. As explained in Section VI, the gains are determined by calculating the ratio of the fundamental components of the battery and the input current obtained through the simulation and from the measurements.

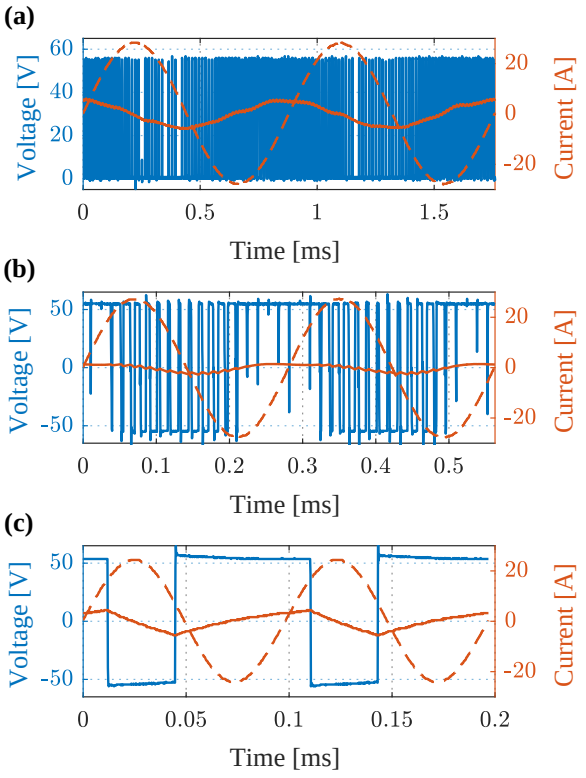

Figure 6. Voltage and currents measurements obtained for the three configurations: a) half-bridge with current control, b) full-bridge with current control, c) full-bridge where the switching frequency is the same as the resonant frequency.

Note that, the values in Table II are given in pairs. The first is always the value used in the simulation ran in PLECS, whereas the second one is the value measured in the experiment. Parameters f_{op}, L_1, L_2, and C_{r} were obtained using the optimization method, and once the components were selected off the shelf, their stray resistances R_{L1}, R_{L2}, and R_C were measured (with the Rohde & Schwarz LCR Bridge and a 1 kHz signal as mentioned in Section VI) for each correspondent case. The gain results obtained in PLECS simulations and the experimental results show good agreement, as it is visible in Table II. For all the studied configurations, voltage and current were measured at the input and output of the VSC, as well as the current in the LIB pack (yellow M1, M2 and M3 symbols found in Figure 2 point at the exact location of the measurements). The measurements were used to compare the

This article has been accepted for publication in a future issue of this journal, but has not been fully edited. Content may change prior to final publication. Citation information: DOI 10.1109/TTE.2019.2920328, IEEE Transactions on Transportation Electrification

Table II
OPERATING FREQUENCIES, COMPONENT VALUES AND OBTAINED GAINS FOR THREE CONFIGURATIONS.

	$f_{\mathbf{op}}$ [Hz]		L_1 [μH]		R_{L1}[mΩ]		L_2 [μH]		R_{L2} [mΩ]		C_{r} [μF]		R_{C} [mΩ]		**Gain**	
Case 1	1139.2	1136	235.3	235.6	40	39.3	59.4	59.4	40	28.6	294.4	294.1	30	6.6	5.5	5.3
Case 2	3568.3	3560	382.3	383.3	55	51.3	60.6	59.4	30	28.6	30.9	29.8	10	6.8	15.8	15.7
Case 3	10179.3	10155	232.7	237.6	40	37.5	7.8	5.9	15	13	30.9	29.7	15	7.3	6.5	6.2

three configurations with each other, to determine the achieved AC current magnification for each of the filters and for a power analysis, presented in the following subsection.

A. Measurements of the semiconductor losses

The following standard equation is used in order to calculate the average active power

$$P_{\mathrm{avg}} = \frac{1}{T}\int_0^T u_{\mathrm{m}}(t) i_{\mathrm{m}}(t) dt \tag{22}$$

with T as the integer number of periods, and $u_{\mathrm{m}}(t)$, $i_{\mathrm{m}}(t)$ as the measured signals at each of the measurement points in the circuit. The main target of these measurements was to record the semiconductor losses, which were obtained by subtracting the calculated VSC output power from the power entering the converter (VSC input) and they are shown in Figure 7.

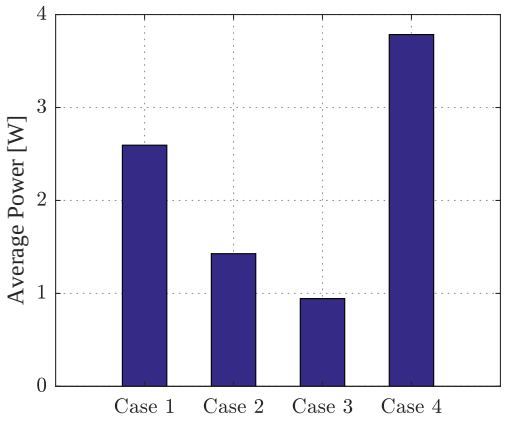

Figure 7. Comparison of the VSC's semiconductor losses for the four studied cases, i.e.: case 1) half-bridge driving i_{in} into an LCL using PWM; case 2) full-bridge driving i_{in} into an LCL using PWM; case 3) full-bridge driving i_{in} into an LCL, where the switching frequency is the resonant frequency; case 4) half-bridge driving i_{in} into an inductor using PWM.

VIII. DISCUSSION OF THE RESULTS

Figure 7 shows the VSC's semiconductor losses obtained for the three configurations from the measurements presented in Figure 6, plus the reference case. All the four cases consider 28 A of injected AC current into the LIB pack under test. Some remarks can be made. First, when compared, the losses of the semiconductors for the half-bridge, considering that six switches are used (according to Section V), tend to be higher than the ones for the full-bridge configuration, which utilizes just four switches. Second, and as it was the goal, by reducing the current in L_1, which is the same as the current in the switches, the losses (due to switching action as well as due to conduction) are therefore reduced. Third, because the full-bridge allows the voltage u_{in} to be the double of the one in the half-bridge, for the same current in the LIB, higher impedances according to (17) are possible. This allows a larger search in the Pareto front, which results in the possibility to privilege gains rather than impedance optima (as presented in Figure 3 from Section IV-C). Finally, considering that the switching frequency of the full-bridge without current modulation is almost seven times smaller than the one used for the full-bridge with current control (70 kHz), it is comprehensible that, for the first configuration, the semiconductors losses are even smaller.

In the presented experimental setup, by comparing the semiconductor losses measured in the reference case (case 4) against the ones produced in the last full-bridge configuration (case 3), one contemplated a reduction of 75%. This result is due to the fact that the semiconductors operate with lower currents and lower switching frequencies. In addition to reducing the stress experienced in the semiconductors, this may potentially also reduce the size of the DC-(DC/X·AC) converter itself.

IX. CONCLUSION

With the purpose of magnifying AC current for generating heat in LIBs, a multi-objective algorithm for DC-DC converter design using transformerless resonant filters is proposed. The multi-objective algorithm may provide optimal resonant filter impedances, as well as, optimal operating frequency for VSCs. Thereby, VSC's output voltage saturation is avoided, the semiconductor's current is reduced, and yet large LIB currents are reached. In the presented experimental setup by using an LCL circuit and a full-bridge switch arrangement, injected AC currents into a LIB with magnifications of up to 15.7 are reached. By matching the switching frequency with the frequency where the LCL and the battery resonate, the current flowing in the semiconductors and the switching frequency could be reduced. This resulted in a loss reduction in the semiconductors of up to 75% when compared with a non-magnified injected AC current.

ACKNOWLEDGMENTS

This work is supported by the Swedish Energy Agency (research grant number 37434-1) and Scania AB.

APPENDIX

A. Computation of the Gain Transfer Function

The transfer function $G_{1,1}(s)$, as shown in (14), corresponds to the admittance of the overall circuit. For the two pole, two

This article has been accepted for publication in a future issue of this journal, but has not been fully edited. Content may change prior to final publication. Citation information: DOI 10.1109/TTE.2019.2920328, IEEE Transactions on Transportation Electrification

zero LIB model and the LCL resonant filter the Gain transfer function can be written as

$$G_{\text{Gain}}(s) = (C_r R_c s + 1)(a_{11}a_{22} - a_{12}a_{21} - (a_{11}+ a_{22})s + s^2)(C_r(L_2 s^4 - (L_2 a_{11} + L_2 a_{22} - R_c - R_{L2} - d_b)s^3) + (1 + (C_r L_2(a_{11}a_{22} - a_{12}a_{21}) + C_r(b_1 c_1 + b_2 c_2) - C_r(a_{11} + a_{22})(R_c + R_{L2} + d_b))s^2 - (a_{11} + a_{22} - C_r((d_b + R_c + R_{L2})(a_{11}a_{22} - a_{12}a_{21}) - (a_{11}b_2c_2 + a_{22}b_1c_1) + (a_{12}b_2c_1 + a_{21}b_1c_2)))s + a_{11}a_{22} - a_{12}a_{21})^{-1}. \quad (23)$$

The coefficients $a_{11,12,21,22}, b_1, b_2, c_1, c_2$ and d_b correspond to the coefficients of the matrix and the vectors describing the cell impedance in (4). The expression (23) was obtained with the help of the mathematical software Maple[7].

REFERENCES

[1] J. Fan and S. Tan, "Studies on Charging Lithium-Ion Cells at Low Temperatures," *Journal of The Electrochemical Society*, vol. 153, pp. A1081–A1092, Jun. 2006.

[2] J. Vetter, P. Novk, M. R. Wagner, C. Veit, K. C. Mller, J. O. Besenhard, M. Winter, M. Wohlfahrt-Mehrens, C. Vogler, and A. Hammouche, "Ageing mechanisms in lithium-ion batteries," *Journal of Power Sources*, vol. 147, pp. 269–281, Sep. 2005.

[3] M. Broussely, P. Biensan, F. Bonhomme, P. Blanchard, S. Herreyre, K. Nechev, and R. J. Staniewicz, "Main aging mechanisms in Li ion batteries," *Journal of Power Sources*, vol. 146, pp. 90–96, Aug. 2005.

[4] I. J. Fernndez, C. F. Calvillo, A. Snchez-Miralles, and J. Boal, "Capacity fade and aging models for electric batteries and optimal charging strategy for electric vehicles," *Energy*, vol. 60, pp. 35–43, Oct. 2013.

[5] T. Waldmann, M. Wilka, M. Kasper, M. Fleischhammer, and M. Wohlfahrt-Mehrens, "Temperature dependent ageing mechanisms in Lithium-ion batteries A Post-Mortem study," *Journal of Power Sources*, vol. 262, pp. 129–135, Sep. 2014.

[6] T. A. Stuart and A. Hande, "HEV battery heating using AC currents," *Journal of Power Sources*, vol. 129, pp. 368–378, Apr. 2004.

[7] J. Zhang, H. Ge, Z. Li, and Z. Ding, "Internal heating of lithium-ion batteries using alternating current based on the heat generation model in frequency domain," *Journal of Power Sources*, vol. 273, pp. 1030–1037, Jan. 2015.

[8] J. Zhu, Z. Sun, X. Wei, and H. Dai, "An alternating current heating method for lithium-ion batteries from subzero temperatures," *International Journal of Energy Research*, vol. 40, pp. 1869–1883, Oct. 2016.

[9] S. Mohan, Y. Kim, and A. G. Stefanopoulou, "Energy-Conscious Warm-Up of Li-Ion Cells From Subzero Temperatures," *IEEE Transactions on Industrial Electronics*, pp. 2954–2964, May 2016.

[10] J. Zhu, Z. Sun, X. Wei, H. Dai, and W. Gu, "Experimental investigations of an AC pulse heating method for vehicular high power lithium-ion batteries at subzero temperatures," *Journal of Power Sources*, vol. 367, pp. 145–157, Nov. 2017.

[11] Y. Shang, B. Xia, N. Cui, C. Zhang, and C. C. Mi, "An Automotive Onboard AC Heater Without External Power Supplies for Lithium-Ion Batteries at Low Temperatures," *IEEE Transactions on Power Electronics*, pp. 7759–7769, Sep. 2018.

[12] D. Kim, Y. Lee, S. Ha, Y. Jang, and G. Moon, "Self-preheating Method for Li-ion Battery Using Battery Impedance Estimator," in *2018 International Power Electronics Conference (IPEC-Niigata 2018 -ECCE Asia)*, May 2018, pp. 3466–3470.

[13] Y. Ji and C. Y. Wang, "Heating strategies for Li-ion batteries operated from subzero temperatures," *Electrochimica Acta*, vol. 107, pp. 664–674, Sep. 2013.

[14] D. Christen, S. Tschannen, and J. Biela, "Highly efficient and compact DC-DC converter for ultra-fast charging of electric vehicles," in *2012 15th International Power Electronics and Motion Control Conference (EPE/PEMC)*, Sep. 2012, pp. LS5d.3–1–LS5d.3–8.

[15] V. Monteiro, J. G. Pinto, B. Exposto, and J. L. Afonso, "Comprehensive comparison of a current-source and a voltage-source converter for three-phase EV fast battery chargers," in *2015 9th International Conference on Compatibility and Power Electronics (CPE)*, Jun. 2015, pp. 173–178.

[7]Maple is a trademark or registered trademark of Waterloo Maple Inc.

[16] J. Lee, Y. Jeong, and B. Han, "A Two-Stage Isolated/Bidirectional DC/DC Converter With Current Ripple Reduction Technique," *IEEE Transactions on Industrial Electronics*, vol. 59, no. 1, pp. 644–646, Jan. 2012.

[17] S. Park, D. Kim, D. Joo, M. Kim, and B. Lee, "Design of output filter in LLC resonant converters for ripple current reduction in battery charging applications," in *2015 9th International Conference on Power Electronics and ECCE Asia (ICPE-ECCE Asia)*, Jun. 2015, pp. 2050–2056.

[18] K. Uddin, A. D. Moore, A. Barai, and J. Marco, "The effects of high frequency current ripple on electric vehicle battery performance," *Applied Energy*, vol. 178, pp. 142–154, Sep. 2016.

[19] D. B. W. Abeywardana, B. Hredzak, J. E. Fletcher, and G. Konstantinou, "A cascaded boost inverter based battery energy storage system with reduced battery ripple current," in *IECON 2017 - 43rd Annual Conference of the IEEE Industrial Electronics Society*, Oct. 2017, pp. 2733–2738.

[20] S. De Breucker, K. Engelen, R. D'hulst, and J. Driesen, "Impact of Current Ripple on Li-Ion Battery Ageing," in *EVS27*, Barcelona, Spain, Nov. 2013.

[21] L. W. Juang, P. J. Kollmeyer, A. E. Anders, T. M. Jahns, R. D. Lorenz, and D. Gao, "Investigation of the influence of superimposed AC current on lithium-ion battery aging using statistical design of experiments," *Journal of Energy Storage*, vol. 11, pp. 93–103, Jun. 2017.

[22] M. J. Brand, M. H. Hofmann, S. F. Schuster, P. Keil, and A. Jossen, "The influence of current ripples on the life-time of lithium-ion batteries," *IEEE Transactions on Vehicular Technology*, 2018.

[23] R. Soares, A. Bessman, O. Wallmark, G. Lindbergh, and P. Svens, "An Experimental Setup with Alternating Current Capability for Evaluating Large Lithium-Ion Battery Cells," *Batteries*, vol. 4, no. 3, p. 38, Aug. 2018.

[24] A. Bessman, R. Soares, O. Wallmark, P. Svens, and G. Lindbergh, "Aging effects of AC harmonics on lithium-ion cells," *Journal of Energy Storage*, vol. 21, pp. 741–749, Feb. 2019.

[25] S. Skoog, "Electro-thermal modeling of high-performance lithium-ion energy storage systems including reversible entropy heat," in *2017 IEEE Applied Power Electronics Conference and Exposition (APEC)*, Mar. 2017, pp. 2369–2373.

[26] T. G. Zavalis, M. Klett, M. H. Kjell, M. Behm, R. W. Lindström, and G. Lindbergh, "Aging in lithium-ion batteries: Model and experimental investigation of harvested LiFePO4 and mesocarbon microbead graphite electrodes," *Electrochimica Acta*, vol. 110, pp. 335–348, Nov. 2013.

[27] T. Reddy, *Linden's Handbook of Batteries, 4th Edition*. McGraw Hill Professional, Jun. 2010.

[28] T. Momma, M. Matsunaga, D. Mukoyama, and T. Osaka, "Ac impedance analysis of lithium ion battery under temperature control," *Journal of Power Sources*, vol. 216, pp. 304–307, Oct. 2012.

[29] X. Hu, S. Li, and H. Peng, "A comparative study of equivalent circuit models for Li-ion batteries," *Journal of Power Sources*, pp. 359–367, Jan. 2012.

[30] H. He, R. Xiong, and J. Fan, "Evaluation of Lithium-Ion Battery Equivalent Circuit Models for State of Charge Estimation by an Experimental Approach," *Energies*, vol. 4, pp. 582–598, Mar. 2011.

[31] S. E. Li, B. Wang, H. Peng, and X. Hu, "An electrochemistry-based impedance model for lithium-ion batteries," *Journal of Power Sources*, vol. 258, pp. 9–18, Jul. 2014.

[32] R. Mohan, Undeland, *Power Electronics converter, Applications and Design*. Hoboken, New Jersey: John Wiley & Sons, 2003.

[33] J. H. Holland, "Genetic algorithms and adaptation," in *Adaptive Control of Ill-Defined Systems*. Springer, 1984, pp. 317–333.